

# Phase diagram and electronic indication of high-temperature superconductivity at 65 K in single-layer FeSe films

Shaolong He<sup>1†</sup>, Junfeng He<sup>1†</sup>, Wenhao Zhang<sup>2,3†</sup>, Lin Zhao<sup>1†</sup>, Defa Liu<sup>1</sup>, Xu Liu<sup>1</sup>, Daixiang Mou<sup>1</sup>, Yun-Bo Ou<sup>3</sup>, Qing-Yan Wang<sup>2,3</sup>, Zhi Li<sup>3</sup>, Lili Wang<sup>3</sup>, Yingying Peng<sup>1</sup>, Yan Liu<sup>1</sup>, Chaoyu Chen<sup>1</sup>, Li Yu<sup>1</sup>, Guodong Liu<sup>1</sup>, Xiaoli Dong<sup>1</sup>, Jun Zhang<sup>1</sup>, Chuangtian Chen<sup>4</sup>, Zuyan Xu<sup>4</sup>, Xi Chen<sup>2</sup>, Xucun Ma<sup>3\*</sup>, Qikun Xue<sup>2\*</sup> and X. J. Zhou<sup>1\*</sup>

The recent discovery of possible high-temperature superconductivity in single-layer FeSe films<sup>1,2</sup> has generated significant experimental and theoretical interest<sup>3,4</sup>. In both the cuprate<sup>5,6</sup> and the iron-based<sup>7–11</sup> high-temperature superconductors, superconductivity is induced by doping charge carriers into the parent compound to suppress the antiferromagnetic state. It is therefore important to establish whether the superconductivity observed in the single-layer sheets of FeSe—the essential building blocks of the Fe-based superconductors—is realized by undergoing a similar transition. Here we report the phase diagram for an FeSe monolayer grown on a SrTiO<sub>3</sub> substrate, by tuning the charge carrier concentration over a wide range through an extensive annealing procedure. We identify two distinct phases that compete during the annealing process: the electronic structure of the phase at low doping (N phase) bears a clear resemblance to the antiferromagnetic parent compound of the Fe-based superconductors, whereas the superconducting phase (S phase) emerges with the increase in doping and the suppression of the N phase. By optimizing the carrier concentration, we observe strong indications of superconductivity with a transition temperature of  $65 \pm 5$  K. The wide tunability of the system across different phases makes the FeSe monolayer ideal for investigating not only the physics of superconductivity, but also for studying novel quantum phenomena more generally.

In high-temperature cuprate superconductors, superconductivity is realized by doping the parent Mott insulator with charge carriers to suppress the antiferromagnetic state<sup>6</sup>. With increasing doping, the material undergoes a transition from an antiferromagnetic insulator, to a superconductor and eventually to a non-superconducting normal metal. In the superconducting region, the transition temperature  $T_c$  can be tuned by the carrier concentration, initially increasing with increasing doping, reaching a maximum at an optimal doping, and then decreasing with further doping<sup>6</sup>. Such a rich evolution with doping not only provides a method to tune the physical properties in a marked way, but also provides clues and constraints in understanding the origin of the high- $T_c$  superconductivity. The same is true for the Fe-based superconductors

where superconductivity is achieved by substitution or doping the parent magnetic compounds, which are nevertheless metallic<sup>12,13</sup>. Again, the superconducting transition temperature can be tuned over a wide doping range with a maximum  $T_c$  at the optimal doping. Understanding this evolution is also a prerequisite to uncovering the origin of high-temperature superconductivity in the Fe-based superconductors.

The latest discovery of a high-temperature superconductivity signature in single-layer FeSe films<sup>1,2</sup> is significant in a number of respects. First, they may exhibit a high  $T_c$  that breaks the  $T_c$  record ( $\sim 55$  K) of Fe-based superconductors reported in 2008 (refs 7–11, 14). Second, the discovery of such a high  $T_c$  in single-layer FeSe films is surprising when considering that their bulk counterpart has a  $T_c$  of only 8 K (ref. 10), although this can be enhanced to 36.7 K under high pressure<sup>15</sup>. Third, it provides an ideal system to investigate the origin of high-temperature superconductivity. On the one hand, this system consists of a single-layer FeSe film that has a simple crystal structure and is strictly two-dimensional (2D); its simple electronic structure may provide key insights into the high- $T_c$  superconductivity mechanism in the Fe-based compounds<sup>2</sup>. On the other hand, the unique properties of this system may involve the interface between the single-layer FeSe film and the SrTiO<sub>3</sub> substrate, that provides an opportunity to investigate the role of the interface in generating high- $T_c$  superconductivity<sup>1</sup>.

As for cuprates and other Fe-based superconductors, it is important to explore whether the single-layer FeSe system can be tuned to vary its physical properties and superconductivity by changing the charge-carrier concentration. Here, we report a wide range tunability of the electronic structure and physical properties that is realized in the single-layer FeSe film. Instead of chemical substitution that is commonly used in most other Fe-based superconductors, the doping here is realized by a simple annealing process. The electronic structure varies markedly during the annealing process. It starts from one end phase (called the N phase) and ends with another different phase (called the S phase), with these two phases competing in the intermediate stage. A signature of superconductivity is observed in the S phase, which varies with doping and when optimized, can reach a record high

<sup>1</sup>National Lab for Superconductivity, Beijing National Laboratory for Condensed Matter Physics, Institute of Physics, Chinese Academy of Sciences, Beijing 100190, China, <sup>2</sup>State Key Lab of Low-Dimensional Quantum Physics, Department of Physics, Tsinghua University, Beijing 100084, China, <sup>3</sup>Beijing National Laboratory for Condensed Matter Physics, Institute of Physics, Chinese Academy of Sciences, Beijing 100190, China, <sup>4</sup>Technical Institute of Physics and Chemistry, Chinese Academy of Sciences, Beijing 100190, China. <sup>†</sup>These authors contributed equally to this work.

\*e-mail: XJZhou@aphy.iphy.ac.cn; qkxue@mail.tsinghua.edu.cn; xcma@aphy.iphy.ac.cn

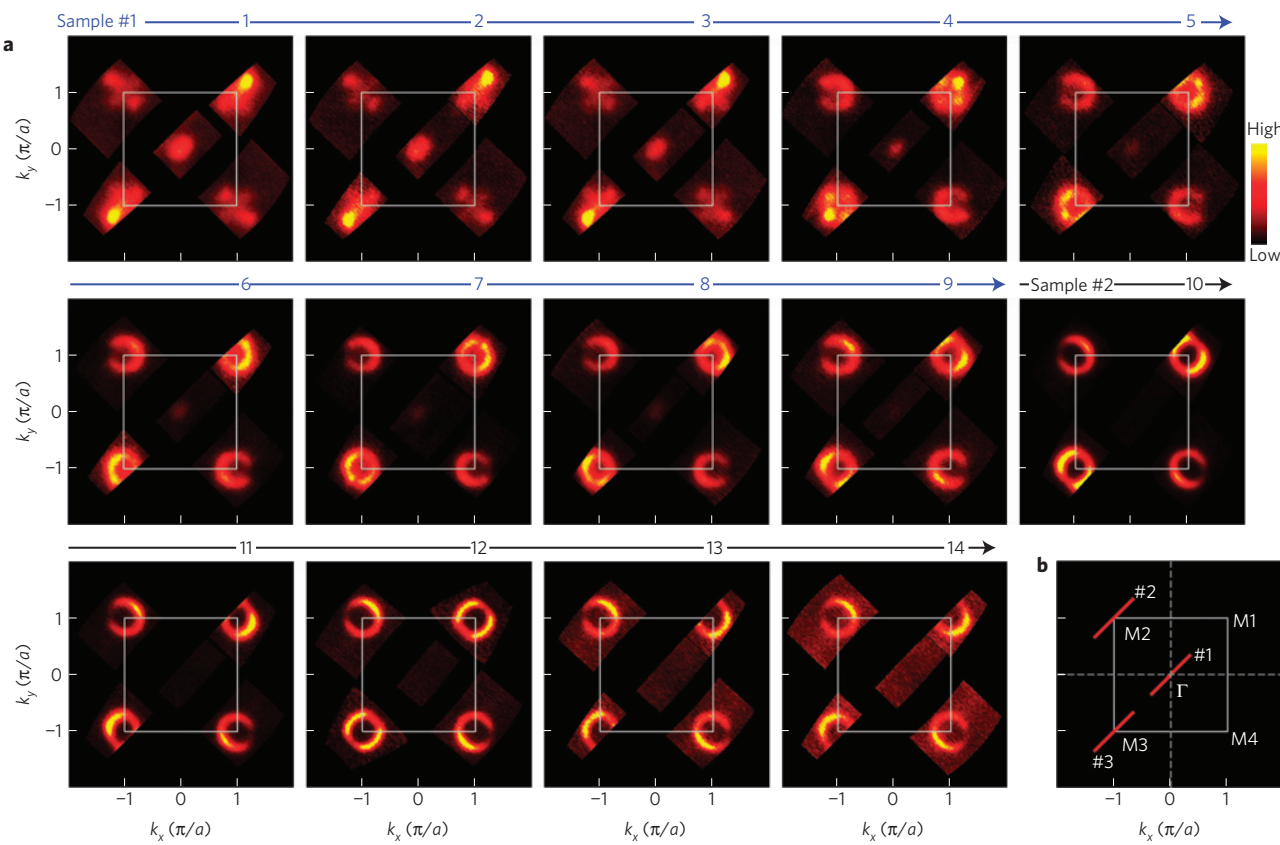


**Figure 1 | Fermi surface evolution of the single-layer FeSe film during the annealing process.** **a**, Integrated spectral intensity as a function of momentum for the single-layer FeSe film from two samples annealed at different stages. For convenience, we use the annealing sequence to denote different samples annealed under different conditions, as indicated in Supplementary Fig. S1. The first 3 images (steps 1–3) are obtained by integrating the spectral weight over a small energy window [−0.03 eV, −0.01 eV] because the observed bands are below the Fermi level. The rest of the images are obtained by integrating over a small energy window [−0.01 eV, 0.01 eV] around the Fermi level. **b**, Labelling of the Brillouin zone; for convenience, the four equivalent M points are labelled as M1( $\pi, \pi$ ), M2( $-\pi, \pi$ ), M3( $-\pi, -\pi$ ) and M4( $\pi, -\pi$ ). The locations of the momentum cuts for the bands measured in Fig. 2 are also marked.

$T_c$  of  $(65 \pm 5)$  K. Such a wide tunability of the single-layer FeSe film not only provides an opportunity to investigate the physics and superconductivity mechanism of the Fe-based superconductors, but also provides an ideal system to fabricate heterostructure devices for new quantum phenomena and potential applications.

The as-prepared single-layer FeSe film grown at relatively low temperature is non-superconducting; superconductivity is realized by the subsequent annealing in vacuum at a relatively high temperature for a period of time<sup>1,2</sup>. To follow the non-superconducting to superconducting transition during the annealing process, we have divided the annealing process into many small steps by gradually increasing the annealing temperature and annealing time (see Supplementary Fig. S1). The samples were *in situ* annealed, and then angle-resolved photoemission (ARPES) was used to measure their band structure, Fermi surface and energy gap after each annealing step (see Supplementary Information and Methods). We note that owing to slight variation in the SrTiO<sub>3</sub> substrates and the initial preparation conditions of the single-layer FeSe thin films, the starting point of the electronic structure may vary between samples. However, their annealing processes all follow the typical trends that are shown in Figs 1 and 2 and eventually come to a similar end point. We have worked on many samples and the results are highly reproducible.

Figure 1 shows the Fermi surface evolution with the annealing process for two single-layer FeSe samples at different annealing stages; they basically span the entire annealing process under our annealing conditions. The corresponding band structures are

shown in Fig. 2. For convenience, we use the annealing sequence to denote different samples annealed under different conditions, as indicated in Supplementary Fig. S1. As seen in Figs 1 and 2, the Fermi surface and the band structure of the single-layer FeSe film experience a pronounced change during the annealing process. To check whether any signal comes from the SrTiO<sub>3</sub> substrate, we prepared a SrTiO<sub>3</sub> substrate using the same procedure used to make the single-layer FeSe thin films, and then annealed the substrate by the same process used for the FeSe films. Our careful ARPES measurements indicate that none of the bands reported in this paper comes from the SrTiO<sub>3</sub> substrate prepared by such a process.

Two distinct phases appeared during the annealing process, as seen from Figs 1 and 2. In the initial stage, the electronic structure of the first three steps (1–3) is similar, which can be attributed to a pure N phase, whose schematic band structure is shown in Fig. 2d (the detailed band structure of the N phase and its corresponding photoemission spectra are shown in Supplementary Fig. S2). We note that the N2 band seems to end abruptly near the Fermi level because, in the initial stage of annealing, the sample is insulating. The spectral weight distribution as a function of momentum is mainly characterized by two strong spots near the M point. There is also some spectral weight near the zone centre  $\Gamma$  due to the N1 band (Fig. 2d) because its top is quite close to the Fermi level. Further annealing leads to the appearance of additional bands, which start from step 4 and become increasingly pronounced with annealing. In the mean time, the bands corresponding to the N phase decrease in intensity, becoming completely invisible at step 10

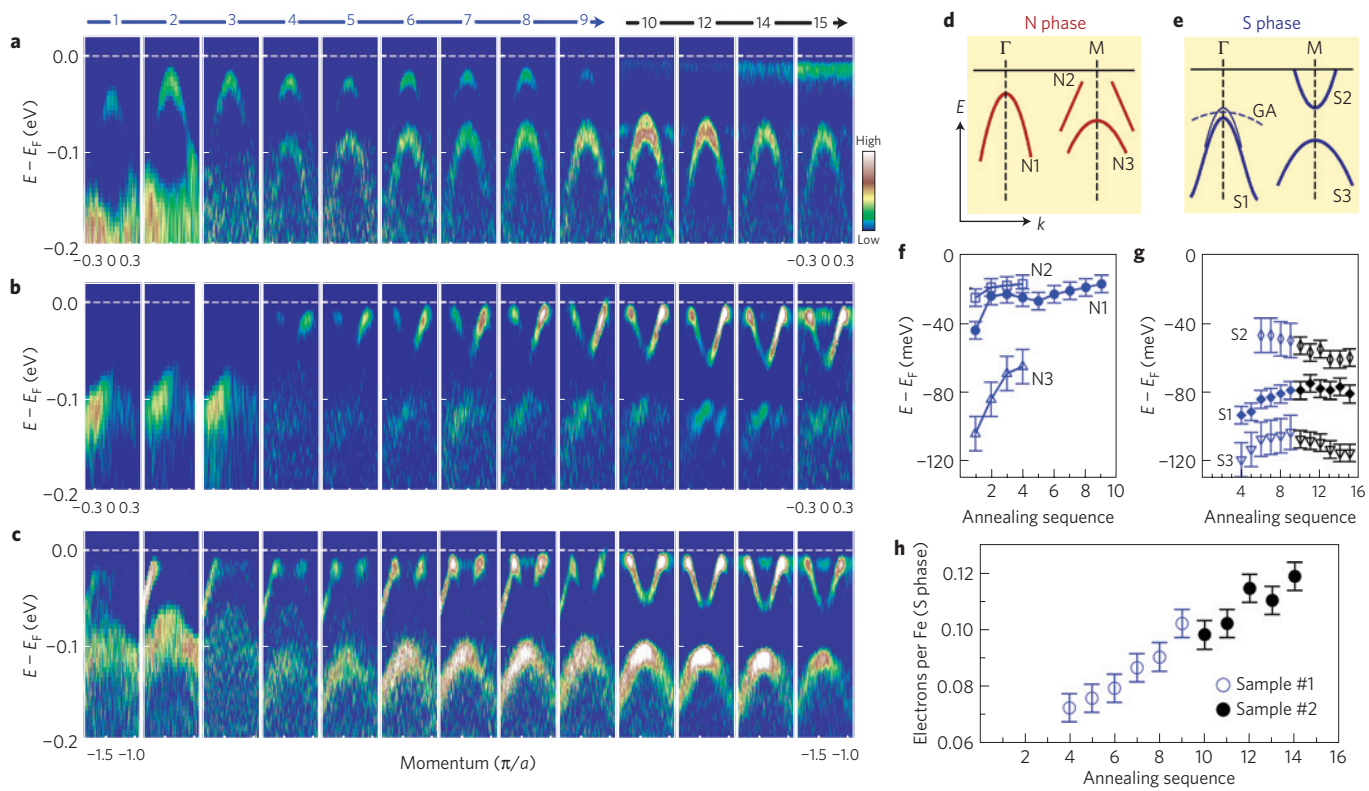


**Figure 2 | Band structure evolution of the single-layer FeSe film during the annealing process.** The images are obtained by the second derivative of the original data with respect to the energy. The original bands and associated photoemission spectra for some typical steps are shown in Supplementary Figs S2–S4. **a**, Evolution of band structure for cut #1 near the zone centre  $\Gamma$  point in Fig. 1b. **b**, Band structure for cut #2 near the M2 point in Fig. 1b. **c**, Band structure for cut #3 near the M3 point in Fig. 1b. **d**, Schematic band structure of the N phase. **e**, Schematic band structure of the S phase. Near the  $\Gamma$  point, in addition to the S1 main band, there is an indication of band splitting near the top of the S1 band, as well as the existence of another flat band labelled as GA, as shown in Supplementary Fig. S3. **f**, Variation of the N1 band top, N2 band top and N3 band top in the N phase, as shown in **d**, during the annealing process. **g**, Variation of the S1 band top, S2 band bottom and S3 band top in the S phase, as shown in **e**, during the annealing process. **h**, Electron counting for the Fe in the S phase as determined from the electron-like Fermi surface size near M by assuming two degenerate Fermi surface sheets near M.

(Fig. 2a–c). The band structure for step 10 and thereafter is similar and can be ascribed to another pure S phase, whose schematic band structure is shown in Fig. 2e (the detailed band structure of the S phase and its corresponding photoemission spectra are shown in Supplementary Fig. S3). The S phase is characterized by an electron-like Fermi surface around the M point (Fig. 1; ref. 2); its band structure (Fig. 2e) shows a clear resemblance to that of  $A_xFe_{2-x}Se_2$  superconductors<sup>16–19</sup>. It seems that the N phase is stable at relatively low annealing temperature whereas the S phase becomes dominant at relatively high annealing temperature. In the intermediate stage, the band structure can be understood as a mixture of the N phase and S phase (the detailed electronic structure of a mixed phase can be seen in Supplementary Fig. S4). The corresponding Fermi surface is also a combination of the N and S phases, with both strong spots and an electron-like Fermi surface near the M point (most notable for steps 4 and 5 in Fig. 1). Although these two phases can coexist in the intermediate stage, they compete with each other in the sense that the S phase increases in intensity with annealing at the expense of the N phase.

In addition to the evolution between the N phase and the S phase, the band structure for a given phase also changes during the annealing process (Fig. 2a–c), signalling a change of the carrier concentration in these two phases. Furthermore, the band structure change shows different trends and magnitudes with the annealing process as plotted in Fig. 2f,g. These indicate that the doping process in both the N phase and the S phase is not a rigid band shift. For the S phase, the doping concentration can be estimated on the basis of the Fermi surface size around the M point. Assuming two degenerate

electron-like Fermi surface sheets near M, the estimated doping of the S phase is shown in Fig. 2h. The S phase is electron-doped and its concentration gradually increases with the annealing process. On the other hand, the effective mass for the electron-like band near M, which can be determined from the band width and the Fermi momentum, is around  $3m_e$  (where  $m_e$  represents the static mass of an electron) and shows little change with doping.

One immediate question arising is what is happening during the annealing process. The change over from one end phase to the other, and the concomitant change of the carrier concentration in a given phase, both indicate that the annealing process has a pronounced effect on the FeSe sample. As the annealing process is rather mild, occurring in a vacuum at relatively low temperature, there are a few possible scenarios. The first is the loss of Se because it evaporates easily; in this case, its loss would give rise to electron doping in the  $FeSe_{1-x}$  system. An indication of Se vacancy in FeSe films grown on graphene substrates has been observed previously from scanning tunnelling microscopy measurements (Fig. 3c in ref. 20). Future work is required to determine whether such Se vacancy, and its variation during the annealing process, can be identified in FeSe films grown on  $SrTiO_3$  substrate. The second possibility is the loss of oxygen near the  $SrTiO_3$  surface; this would also lead to electron doping that can be transferred to FeSe near the interface. Whether the oxygen loss could be significant enough at such a low annealing temperature remains to be investigated. The rearrangement of Fe and Se atoms on the  $SrTiO_3$  surface during annealing is also a possibility. Further experimental and theoretical efforts are required to determine the exact mechanism of the annealing process.

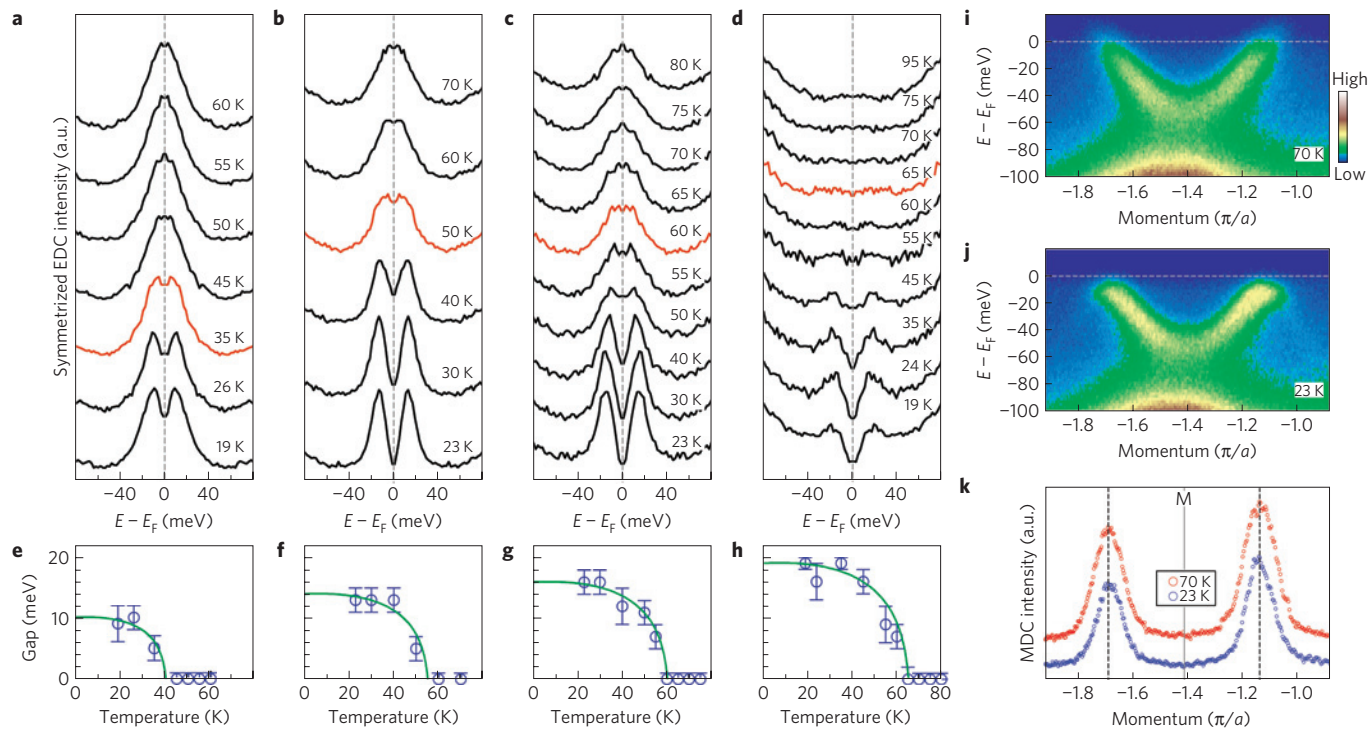


**Figure 3 | Temperature dependence of the energy gap of the single-layer FeSe film annealed under different conditions.** **a-d**, Symmetrized EDCs for the electron-like Fermi surface near the M point at different temperatures for annealing steps 10, 12, 13 and 15, respectively. As noted in the Supplementary Information, the sample temperature has been calibrated. **e-h**, The temperature dependence of the measured energy gap for the above four steps. The gap is obtained by picking the position of the symmetrized EDCs relative to the Fermi level or fitting the symmetrized EDCs with the phenomenological formula that has been commonly used for extracting the energy gap in cuprate superconductors<sup>27</sup>. The green lines represent the best fit between the measured data and the BCS gap form with two fitting parameters,  $T_c$  and the gap size at zero temperature. **i,j**, Band structure along cut #3 in Fig. 1b for step 12 measured at 70 and 23 K, respectively. The corresponding MDCs at the Fermi energy for the two measurements are shown in **k**. The two MDC peaks show little change in their positions above and below the gap opening temperature (~55 K).

The band structure and the spectral weight distribution of the N phase near the M point exhibit a clear resemblance to those of the parent  $\text{AEFe}_2\text{As}_2$  ( $\text{AE} = \text{Ba}$  or  $\text{Sr}$ ) compounds in the magnetic state<sup>21–24</sup> (see Supplementary Fig. S5). The band structure of the N phase is characterized by a hole-like band near M, labelled as N2 in Fig. 2d. A similar hole-like band is also observed in  $\text{AEFe}_2\text{As}_2$  ( $\text{AE} = \text{Ba}$  or  $\text{Sr}$ ) in the magnetic state<sup>21–24</sup>. We note that in the N phase of the single-layer FeSe film, this band initially does not cross the Fermi level, with its peak position of photoemission spectra (energy distribution curves, EDCs) nearly 25 meV below the Fermi level (step 1 in Fig. 2c,f). Further annealing seems to make the N2 band come closer to the Fermi level and eventually get mixed with the electron-like band near M. The spectral weight distribution as a function of momentum for the N phase shows a strong-spots-like feature. This is similar to that observed in  $\text{AEFe}_2\text{As}_2$  ( $\text{AE} = \text{Ba}$  or  $\text{Sr}$ ) in the magnetic state<sup>22,23</sup>. However, in terms of the band structure near  $\Gamma$ , the N phase of the single-layer FeSe is quite different from that of  $\text{AEFe}_2\text{As}_2$  ( $\text{AE} = \text{Ba}$  or  $\text{Sr}$ ) compounds. Whereas there are clear hole-like Fermi surface sheets around  $\Gamma$  in magnetic  $\text{BaFe}_2\text{As}_2$  and  $\text{SrFe}_2\text{As}_2$  (refs 22,23), the bands around  $\Gamma$  in the N phase are below the Fermi level without Fermi crossing. At present, the exact crystal structure and the physical properties of the N phase remain unclear; we will leave this for future investigation.

The single-layer FeSe film on the  $\text{SrTiO}_3$  substrate exhibits one peculiar electronic characteristic in that the bands near the  $\Gamma$  point are all pushed below the Fermi level. This is the case for both the S phase and the N phase when they are compared with the hole-like bands near the  $\Gamma$  in the bulk  $\text{Fe}(\text{Se},\text{Te})$  (ref. 25) and  $\text{BaFe}_2\text{As}_2$  in the magnetic state<sup>23</sup>, respectively. On the other hand, near the M point, the electronic structure of the N phase shows a

resemblance to that of the magnetic state of  $\text{BaFe}_2\text{As}_2$  and the S phase shows a resemblance to that of the bulk  $\text{Fe}(\text{Se},\text{Te})$ . Such a disparity in the electronic behaviour between the  $\Gamma$  and M points in the single-layer FeSe film cannot be explained simply by a rigid band shift due to electron doping in the FeSe film; it does not happen in bulk  $\text{Fe}(\text{Se},\text{Te})$  (ref. 25) or  $\text{Ba}(\text{Fe},\text{Co})_2\text{As}_2$  (ref. 26) systems with similar doping. The first-principles band structure calculations cannot provide a consistent explanation for these observations either<sup>3</sup>. They point to a mechanism that should be closely related to the  $\text{SrTiO}_3$  substrate, be it a strain exerted on the FeSe film from the  $\text{SrTiO}_3$  substrate, or electric polarizability of the dielectric  $\text{SrTiO}_3$ , or the effect of the FeSe– $\text{SrTiO}_3$  interface<sup>4</sup>. Understanding the origin of this peculiar electronic characteristic of the single-layer FeSe film on  $\text{SrTiO}_3$  substrate will be important to understand its unusual physical properties.

Now we discuss the observation and optimization of the high-temperature superconductivity in the S phase. The tunability of the carrier concentration of the S phase by a simple annealing procedure offers an opportunity to investigate the evolution of its electronic structure and particularly its superconductivity with doping. We measured the superconducting gap and its temperature dependence in a single-layer FeSe film annealed at different stages (step 10 and later) with only the pure S phase (Fig. 3). In this case, the relatively high  $T_c$  makes it feasible for us to perform the measurements, and it can also avoid complications from another N phase. To visually inspect possible gap opening and remove the effect of the Fermi distribution function near the Fermi level, Fig. 3a–d shows symmetrized photoemission spectra (EDCs) for the Fermi surface measured at different temperatures, following the procedure commonly used in the study of high-temperature

cuprate superconductors<sup>27</sup>. The gap opening is characterized by a spectral dip at the Fermi level in the symmetrized EDCs. The gap size is determined by the EDC peak position relative to the Fermi level or can be extracted by fitting the symmetrized EDCs with the phenomenological formula proposed in cuprate superconductors<sup>27</sup>; similar results are obtained by these two methods (see Supplementary Fig. S7). We note that this general method of gap extraction has been developed and used in cuprate and Fe-based superconductors for many years. It has been well tested in superconductors whose  $T_c$  is known through other measurements. Therefore, our determination of the gap size and electronic indication of  $T_c$  in the single-layer FeSe film should be reliable. The measured gap size and its temperature dependence, extracted from Fig. 3a–d, are shown in Fig. 3e–h, respectively. The gap size increases with annealing step, from  $\sim 10$  meV for step 10 to  $\sim 19$  meV for step 15. In the mean time, the gap closing temperature also increases from nearly 40 K for step 10 to nearly 65 K for step 15. For a given step, the dependence of the gap size as a function of temperature basically follows a standard Bardeen–Cooper–Schrieffer (BCS) form, as seen from the green lines in Fig. 3e–h.

The energy gap we have observed in the S phase has been attributed to a superconducting gap. It is natural to ask whether it could be any other type of gap. To determine the nature of the gap, we have investigated its momentum dependence<sup>2</sup> and temperature dependence in detail (Fig. 3i–k and see Supplementary Fig. S6). We have determined the Fermi momentum both above and below the transition temperature by various methods, including momentum distribution curves (MDCs; Fig. 3k) and minimum energy gap locus at low temperature, as well as the EDC method to determine the dispersion (Supplementary Fig. S6). We find that the Fermi momentum determined by various methods is consistent, and it remains at the same location both above and below the transition. So far, the superconducting gap is the only known case in which the gap opens along the entire Fermi surface and it is symmetric with respect to the Fermi level owing to the formation of Bogoliubov quasi-particles. This is distinct from other transitions such as spin-density waves or charge-density waves in which only the portion of the Fermi surface that satisfies the perfect nesting condition will open a gap<sup>28,29</sup>; for the rest of the Fermi surface, the Fermi momentum usually exhibits a pronounced difference across the transition temperature<sup>30</sup>. Therefore, our observations strongly indicate that the gap we have observed most likely corresponds to a superconducting gap. Furthermore, the nearly BCS-like form of the temperature dependence of the gap indicates that it is unlikely to be a pseudogap, as observed in cuprates<sup>31</sup>. Direct resistivity and magnetic susceptibility measurements on the single-layer FeSe films are still under way owing to technical difficulties, although transport measurements on a five-layer FeSe film proved that it is superconducting<sup>1</sup>. Our ARPES measurements on the energy gap provide more direct evidence of the high-temperature superconductivity realized in the single-layer FeSe system.

An intriguing issue that arises is whether one should treat the single-layer FeSe film on the SrTiO<sub>3</sub> substrate as predominantly an isolated 2D FeSe system or as a complex interface system with an important interaction between the single-layer FeSe film and the SrTiO<sub>3</sub> substrate. In a strict 2D system, one would expect a Kosterlitz–Thouless transition<sup>32</sup> instead of a true superconducting transition. Although this question needs further investigation, the fact that the single-layer FeSe film on the SrTiO<sub>3</sub> substrate exhibits markedly different behaviours from the bulk FeSe (ref. 10) and even the FeSe thin films on the graphene substrate<sup>20</sup> indicates that the SrTiO<sub>3</sub> substrate and the interface must play an important role.

High-temperature superconductivity with a  $T_c$  as high as  $(65 \pm 5)$  K can be realized in single-layer FeSe under an optimized annealing condition. As shown in Fig. 3, both the  $T_c \sim 60$  K

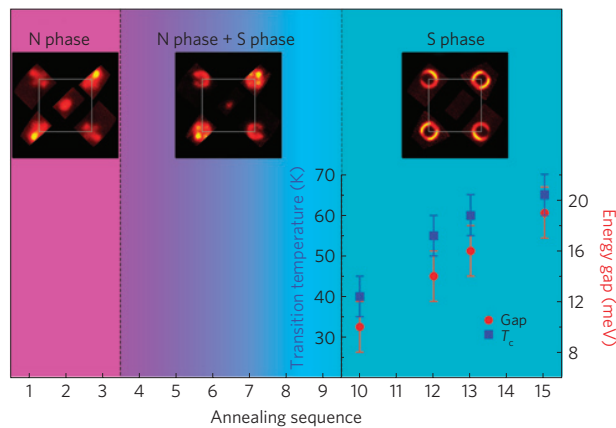


**Figure 4 | Schematic phase diagram of the single-layer FeSe film during the annealing process.** Two end phases are identified, with the nearly pure N phase at the initial stage (steps 1–3), the S phase at the final annealing stage (steps 10–15), and a combination of the N phase and the S phase in between (steps 4–9). Representative Fermi surface maps are shown in the top for the three different regions. In the pure S phase, the measured energy gap size ( $\Delta$ , solid red circles) and the transition temperatures ( $T_c$ , solid blue squares) are shown for different steps; the  $2\Delta/k_B T_c$  is near 6–7.

for step 13 and the  $T_c \sim 65$  K for step 15 have exceeded the transition temperature record ( $\sim 55$  K; ref. 8) reported for Fe-based superconductors. The maximum gap size observed from our ARPES measurements ( $\sim 19$  meV) is quite close to that measured from the scanning tunnelling microscopy/spectroscopy measurements ( $\sim 20$  meV; ref. 1). We note that, although the sample quality improves with annealing at the initial stage, as signalled by the sharpening of the superconducting quasi-particle peak at low temperature (Fig. 3b,c), further annealing leads to a deterioration in the quality of the sample, as seen from the peak broadening and particularly the signal weakening (Fig. 3d). This indicates that the single-layer FeSe film becomes unstable in the final stage of annealing, which prevented us from achieving even higher levels of doping.

Figure 4 schematically summarizes a phase diagram to illustrate the evolution of the electronic structure of the single-layer FeSe film during the annealing process. In particular, the evolution of the superconducting gap ( $\Delta$ ) and that of the superconducting transition temperature are shown in the pure S phase. Both the superconducting gap and the transition temperature increase with the annealing process, giving a ratio  $2\Delta/k_B T_c$  of the order of 6–7. This indicates that the superconductivity in the single-layer FeSe films is in the strong-coupling regime.

The present work demonstrates that the electronic structure and physical properties of the single-layer FeSe film can be tuned continuously over a wide range. By a simple mild annealing process, it can even vary from one end phase to the other with different electronic structures. A  $T_c$  of  $(65 \pm 5)$  K can be realized in the system under an optimized annealing conditions. Although the present work has not spanned the doping level of the S phase all the way to the over-doped region, the phase diagram obtained is similar to that of other Fe-based superconductors, and already contains important information for understanding the physics and superconductivity of the Fe-based superconductors. The existence of two distinct phases, and the tunability of the superconducting properties of the S phase, provide an ideal platform for making heterostructure devices that are needed for both basic studies and potential applications. These include possible combinations of a superconductor with a non-superconductor<sup>33</sup>, and superconductors with other quantum materials such as topological insulators<sup>34,35</sup>.

Received 22 November 2012; accepted 5 April 2013;  
published online 26 May 2013

## References

- Wang, Q. Y. *et al.* Interface-induced high-temperature superconductivity in single unit-cell FeSe films on SrTiO<sub>3</sub>. *Chin. Phys. Lett.* **29**, 037402 (2012).
- Liu, D. F. *et al.* Electronic origin of high-temperature superconductivity in single-layer FeSe superconductor. *Nature Commun.* **3**, 931 (2012).
- Liu, K. *et al.* Atomic and electronic structures of FeSe monolayer and bilayer thin films on SrTiO<sub>3</sub>(001): First-principles study. *Phys. Rev. B* **85**, 235123 (2012).
- Xiang, Y. Y. *et al.* High-temperature superconductivity at the FeSe/SrTiO<sub>3</sub> interface. *Phys. Rev. B* **86**, 134508 (2012).
- Bednorz, J. G. & Mueller, K. A. Possible high  $T_c$  superconductivity in the Ba-La-Cu-O System. *Z. Phys. B* **64**, 189–193 (1986).
- Lee, P. A., Nagaosa, N. & Wen, X. G. Doping a Mott insulator: Physics of high temperature superconductivity. *Rev. Mod. Phys.* **78**, 17–85 (2006).
- Kamihara, Y. *et al.* Iron-based layered superconductor La[O<sub>1-x</sub>F<sub>x</sub>]FeAs ( $x = 0.05\text{--}0.12$ ) with  $T_c = 26$  K. *J. Am. Chem. Soc.* **130**, 3296–3297 (2008).
- Ren, Z. A. *et al.* Superconductivity at 55 K in iron-based F-doped layered quaternary compound Sm[O<sub>1-x</sub>F<sub>x</sub>]FeAs. *Chin. Phys. Lett.* **25**, 2215–2216 (2008).
- Rotter, M. *et al.* Superconductivity at 38 K in the iron arsenide (Ba<sub>1-x</sub>K<sub>x</sub>)Fe<sub>2</sub>As<sub>2</sub>. *Phys. Rev. Lett.* **101**, 107006 (2008).
- Hsu, F. C. *et al.* Superconductivity in the PbO-type structure  $\alpha$ -FeSe. *Proc. Natl Acad. Sci. USA* **105**, 14262–14264 (2008).
- Wang, X. C. *et al.* The superconductivity at 18 K in LiFeAs system. *Solid State Commun.* **148**, 538–540 (2008).
- Paglione, J. & Greene, R. L. High temperature superconductivity in iron-based materials. *Nature Phys.* **6**, 645–658 (2010).
- Wang, F. & Lee, D. H. The electron pairing mechanism of iron-based superconductors. *Science* **332**, 200–204 (2011).
- Guo, J. G. *et al.* Superconductivity in the iron selenide K<sub>x</sub>Fe<sub>2</sub>Se<sub>2</sub> ( $0 \leq x \leq 1.0$ ). *Phys. Rev. B* **82**, 180520(R) (2010).
- Medvedev, S. *et al.* Electronic and magnetic phase diagram of  $\beta$ -Fe<sub>1.01</sub>Se with superconductivity at 36.7 K under pressure. *Nature Mater.* **8**, 630–633 (2009).
- Zhang, Y. *et al.* Nodeless superconducting gap in A<sub>x</sub>Fe<sub>2</sub>Se<sub>2</sub> (A = K, Cs) revealed by angle-resolved photoemission spectroscopy. *Nature Mater.* **10**, 273–277 (2011).
- Mou, D. X. *et al.* Distinct Fermi surface topology and nodeless superconducting gap in a Tl<sub>0.58</sub>Rb<sub>0.42</sub>Fe<sub>1.72</sub>Se<sub>2</sub> superconductor. *Phys. Rev. Lett.* **106**, 107001 (2011).
- Zhao, L. *et al.* Common Fermi-surface topology and nodeless superconducting gap of K<sub>0.68</sub>Fe<sub>1.79</sub>Se<sub>2</sub> and (Tl<sub>0.45</sub>K<sub>0.34</sub>)Fe<sub>1.84</sub>Se<sub>2</sub> superconductors revealed via angle-resolved photoemission. *Phys. Rev. B* **83**, 140508(R) (2011).
- Qian, T. *et al.* Absence of a holelike Fermi surface for the iron-based K<sub>0.8</sub>Fe<sub>1.7</sub>Se<sub>2</sub> superconductor revealed by angle-resolved photoemission spectroscopy. *Phys. Rev. Lett.* **106**, 187001 (2011).
- Song, C. L. *et al.* Molecular-beam epitaxy and robust superconductivity of stoichiometric FeSe crystalline films on bilayer graphene. *Phys. Rev. B* **84**, 020503(R) (2011).
- Yang, L. X. *et al.* Electronic structure and unusual exchange splitting in the spin-density-wave state of the BaFe<sub>2</sub>As<sub>2</sub> parent compound of iron-based superconductors. *Phys. Rev. Lett.* **102**, 107002 (2009).
- Liu, H. Y. *et al.* Fermi surface and band renormalization of Sr<sub>1-x</sub>K<sub>x</sub>Fe<sub>2</sub>As<sub>2</sub> from angle-resolved photoemission spectroscopy. *Phys. Rev. B* **78**, 184514 (2008).
- Liu, G. D. *et al.* Band-structure reorganization across the magnetic transition in BaFe<sub>2</sub>As<sub>2</sub> seen via high-resolution angle-resolved photoemission. *Phys. Rev. B* **80**, 134519 (2009).
- Richard, P. *et al.* Observation of Dirac cone electronic dispersion in BaFe<sub>2</sub>As<sub>2</sub>. *Phys. Rev. Lett.* **104**, 137001 (2010).
- Tamaï, A. *et al.* Strong electron correlations in the normal state of the iron-based FeSe<sub>0.42</sub>Te<sub>0.58</sub> superconductor observed by angle-resolved photoemission spectroscopy. *Phys. Rev. Lett.* **104**, 097002 (2010).
- Liu, C. *et al.* Evidence for a Lifshitz transition in electron-doped iron arsenic superconductors at the onset of superconductivity. *Nature Phys.* **6**, 419–423 (2010).
- Norman, M. R. *et al.* Phenomenology of the low-energy spectral function in high- $T_c$  superconductors. *Phys. Rev. B* **57**, R11093 (1998).
- Gruener, G. The dynamics of spin density waves. *Rev. Mod. Phys.* **66**, 1–24 (1994).
- Gruener, G. The dynamics of charge density waves. *Rev. Mod. Phys.* **60**, 1129–1181 (1988).
- He, R. H. *et al.* From a single-band metal to a high-temperature superconductor via two thermal phase transitions. *Science* **331**, 1579–1583 (2011).
- Timusk, T. & Statt, B. The pseudogap in high-temperature superconductors: An experimental survey. *Rep. Prog. Phys.* **62**, 61–122 (1999).
- Kosterlitz, J. M. & Thouless, D. J. Ordering, metastability and phase transitions in two-dimensional systems. *J. Phys. C* **6**, 1181–1203 (1973).
- Bozovic, I. *et al.* No mixing of superconductivity and antiferromagnetism in a high temperature superconductor. *Nature* **422**, 873–875 (2003).
- Fu, L. & Kane, C. L. Superconducting proximity effect and Majorana fermions at the surface of a topological insulator. *Phys. Rev. Lett.* **100**, 096407 (2008).
- Wang, M. X. *et al.* The coexistence of superconductivity and topological order in the Bi<sub>2</sub>Se<sub>3</sub> thin films. *Science* **336**, 52–55 (2012).

## Acknowledgements

We thank D.-H. Lee and Z.-X. Shen for discussions. X.J.Z. acknowledges financial support from the NSFC (10734120) and the MOST of China (973 programme No: 2011CB921703 and 2011CB605903). Q.X. and X.M. acknowledge support from the MOST of China (programme No. 2009CB929400 and No. 2012CB921702).

## Author contributions

S.H., J.H., W.Z. and L.Z. contributed equally to this work. X.J.Z., Q.X. and X.M. proposed and designed the research. W.Z., Y.-B.O., Q.-Y.W., Z.L., L.W., X.C., X.C.M and Q.X. contributed to MBE thin-film preparation. S.H., J.H., L.Z., D.L., X.L., D.M., Y.P., Y.L., C.C., L.Y., G.L., X.D., J.Z., C.C., Z.X. and X.J.Z. contributed to the development and maintenance of the laser-ARPES system. S.H., J.H., W.Z., L.Z., D.L., X.L. and Y.-B.O. carried out the experiment. S.H., J.H., L.Z., D.L., X.L. and X.J.Z. analysed the data. X.J.Z. wrote the paper with J.H., S.H., L.Z., D.L., X.L., X.M. and Q.X.

## Additional information

Supplementary information is available in the online version of the paper. Reprints and permissions information is available online at [www.nature.com/reprints](http://www.nature.com/reprints). Correspondence and requests for materials should be addressed to X.M., Q.X. or X.J.Z.

## Competing financial interests

The authors declare no competing financial interests.